Supporting Information for "Monitoring Shelf Sea Dynamics with Ocean-Bottom Distributed Acoustic Sensing"

Loïc Viens[1] Zack J. Spica[2], Brent G. Delbridge[1], and Brian K. Arbic [2]

[1]Los Alamos National Laboratory, Los Alamos, New Mexico, USA

[2]Department of Earth and Environmental Sciences, University of Michigan, Ann Arbor, Michigan, USA

Contents of this file

1. Text S1 to S7

2. Figures S1 to S7

Text S1.

NDBC buoy 46229 is close to the fiber-optic cable, but a maintenance event prevented the data from being recorded between October 10 and November 14, 2021. In Figure S1, we show the wave height waveforms recorded at NDBC buoys 46229 and 46050 (locations in Figure 1). While the two buoys are located ∼100 km from each other, their water depths are relatively similar (180 m for buoy 46229 and 160 m for buoy 46050). The wave height

---

March 13, 2023, 3:52pm

waveforms are very similar as the two buoys are located above similar water depths, and we primarily use the continuous data from buoy 46050 in the main manuscript.

Text S2.

To separate the landward and oceanward propagating OSGWs, we apply a f-k filter to each 10-min time series. In Figures S2a-b, we show an example of 10-min $f - k$ filtered time series along the cable, which characterize the landward and oceanward propagating OSGWs. For each virtual source-receiver pair, we compute cross-correlation functions (CCFs) from both landward and oceanward $f - k$ filtered 10-min time windows in the frequency domain as

$$\text{CCF}_{v-r}(t) = F^{-1}\left(\frac{\hat{s}_r \hat{s}_v^*}{\{|\hat{s}_v|\}\{|\hat{s}_r|\}}\right), \tag{1}$$

where $\hat{s}_v$ and $\hat{s}_r$ are the Fourier transform of 10-min f-k filtered strain-rate records at the virtual source (s_v) and receiver (s_r) channels, respectively. The $*$ symbol represents the complex conjugate. The denominator of Equation 1 (i.e., $\{|\hat{s}_v|\}\{|\hat{s}_r|\}$) represents spectral whitening, where $\{\cdot\}$ is a smoothing of the absolute amplitude spectrum ($|\cdot|$) using a running-mean average algorithm over 30 discrete frequency samples (Bensen et al., 2007). The inverse Fourier transform (F^{-1}) is finally applied to retrieve the 10-min CCFs in the time domain.

Examples of CCFs computed between channel 1000 (virtual source) and all the nearby channels (receivers) are shown in Figures S2c–d. Both landward (Figure S2c) and oceanward (Figure S2d) propagating waves can be observed in the 10-min CCFs. Note that only the CCF computed between each virtual source and the 15th channel before the

virtual source is used in the main manuscript (e.g., CCF between virtual source 1000 and receiver 985).

To increase the signal-to-noise ratio, we stack the CCFs over four hours using a phase-weighted stack approach with a power of 2 and a smoothing of 0.5 s (Schimmel & Paulssen, 1997).

Text S3.

We show the correlation coefficients (CCs) after stretching along the cable for the four months of data in Figure S3a. Only the dt/t results with CCs after stretching higher than 0.4 are analyzed in the main manuscript. We illustrate the spatio-temporal dt/t data selection with a binary representation of the CCs after stretching (i.e., CC values higher and lower than 0.4) in Figure S3b. Finally, we show a histogram of the CC values in Figure S3c, which highlights that 94.4% of the CC after stretching values are above 0.4.

Text S4.

We show the bathymetry and its slope along the cable in Figure S4. The slope is computed along the array using a sliding horizontal distance of 500 m. Offshore, the largest slopes are observed between 6.3-12 km, 12-20 km, and after 40 km from the IU.

Text S5.

In the main manuscript, we focus on two regions of the cable where an oceanward surface flow is observed (i.e., dt/t values of -0.04 s). The water depths for these two regions are 79 and 206 m (i.e., 16.9 and 47.5 km from the IU). For such water depths, OSGWs with wavelengths of 158 and 412 m, or wavenumbers of 0.0063 and 0.0024 m^{-1}, respectively,

should theoretically start feeling the bottom of the ocean. In Figure S5, we show daily f-k spectra of the data at those two locations. Between 16.4 and 17.4 km from the IU (Figure S5a), the highest energy level for wind waves (i.e., above 0.1 Hz) is found for a wavenumber of 0.006 m^{-1}, which is very close to the 0.0063 m^{-1} theoretical value. Between 47 and 48 km from the IU (Figure S5b), the maximum energy, which corresponds to the swell energy, is found at a frequency of 0.06 Hz and a wavenumber of 0.002 m^{-1}, which is also very close to the theoretical wavenumber value of 0.0024 m^{-1}. This analysis shows that incoming waves with the most energy start feeling the bottom of the ocean at these two locations, which likely decreases their velocities. The shoaling of incoming waves is likely responsible for the oceanward flow of the ocean's near surface at these two locations.

Text S6.

We show the hourly wind direction and speed recorded at NDBC buoy 46050 in Figure S6. The wind is primarily coming from the North in August and September. In October and November, a clear change of the wind direction can be observed, with winds primarily blowing from the South.
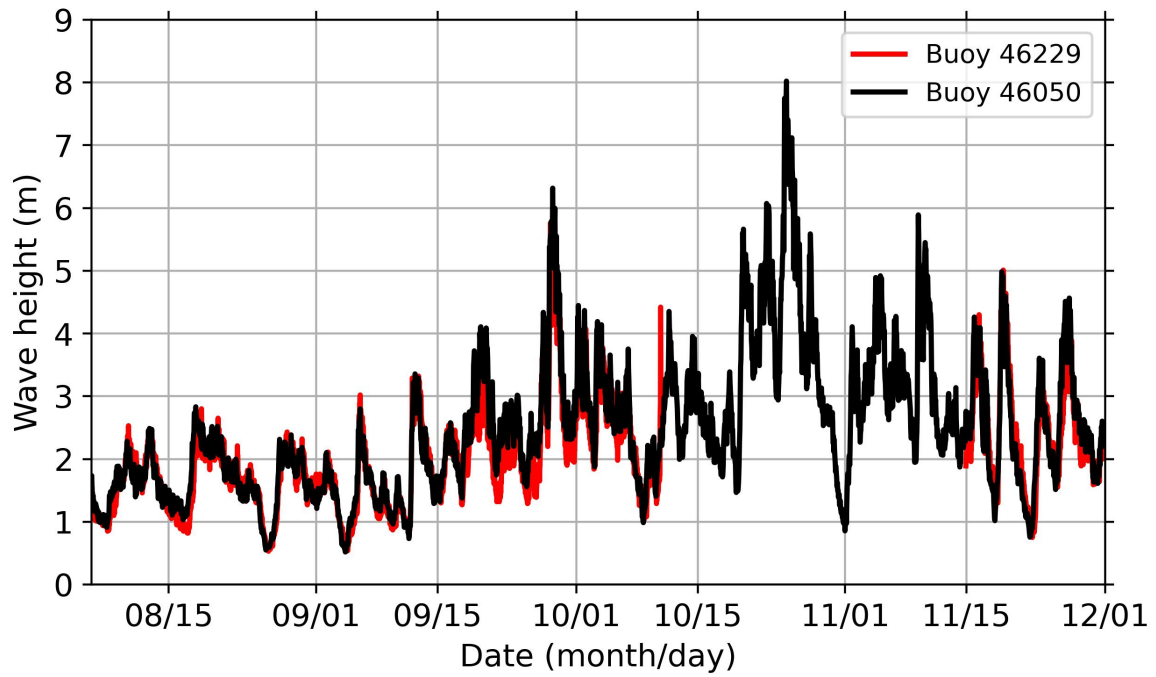
Text S7.

In Figure S7, we show a comparison of the tide gauge data recorded in South Beach, OR, and the high-frequency surface current measurements near the fiber-optic cable. Rising and falling tides generally correlate with stronger landward and oceanward surface currents measured by the high-frequency radar.
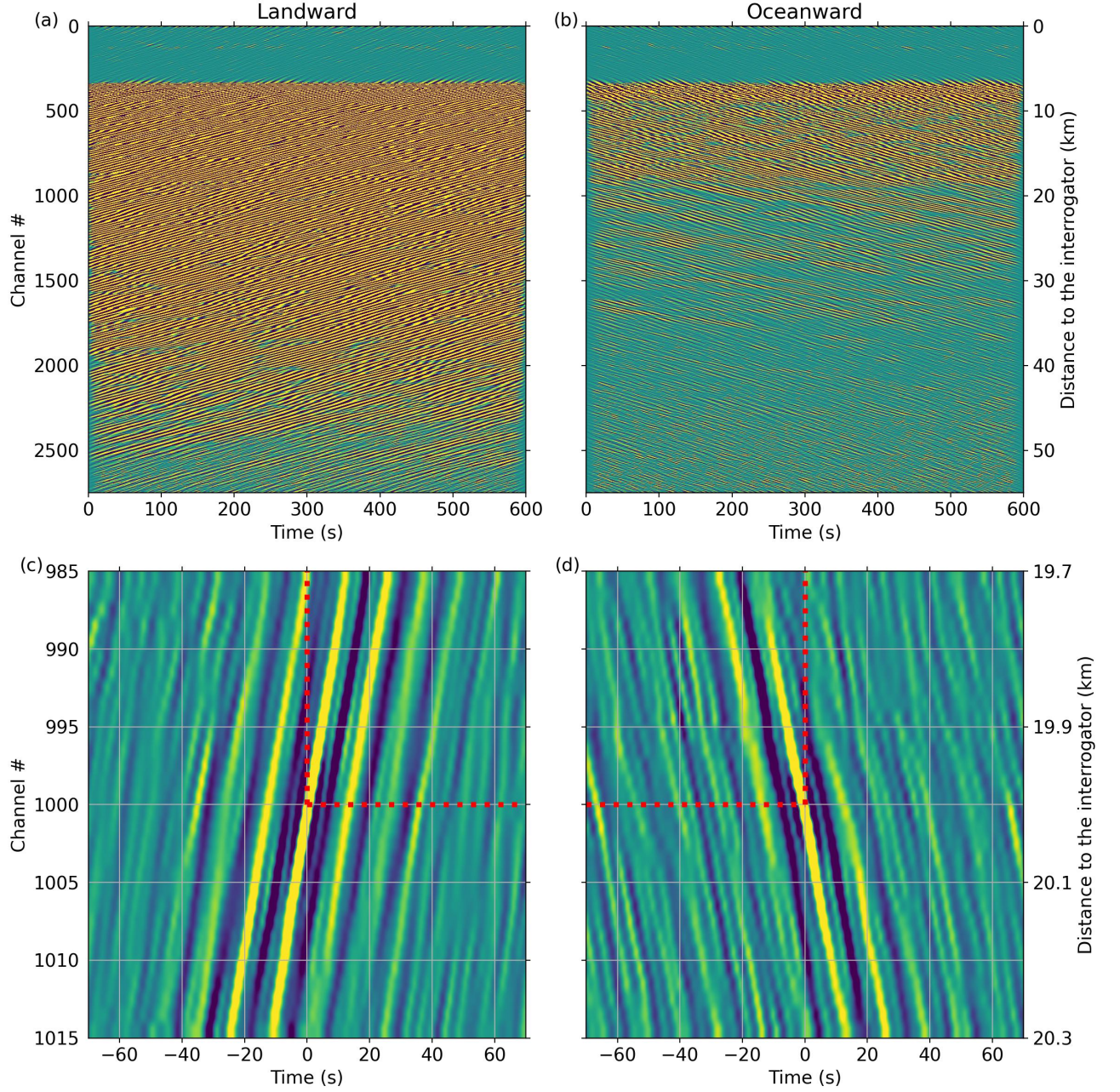
References

 Bensen, G. D., Ritzwoller, M. H., Barmin, M. P., Levshin, A. L., Lin, F., Moschetti,

M. P., ... Yang, Y. (2007). Processing seismic ambient noise data to obtain reliable broad-band surface wave dispersion measurements. *Geophys. J. Int.*, *169*, 1239–1260. doi: 10.1111/j.1365-246X.2007.03374.x

Schimmel, M., & Paulssen, H. (1997). Noise reduction and detection of weak, coherent signals through phase-weighted stacks. *Geophys. J. Int.*, *130*, 497-505. doi: 10.1111/ j.1365-246X.1997.tb05664.x
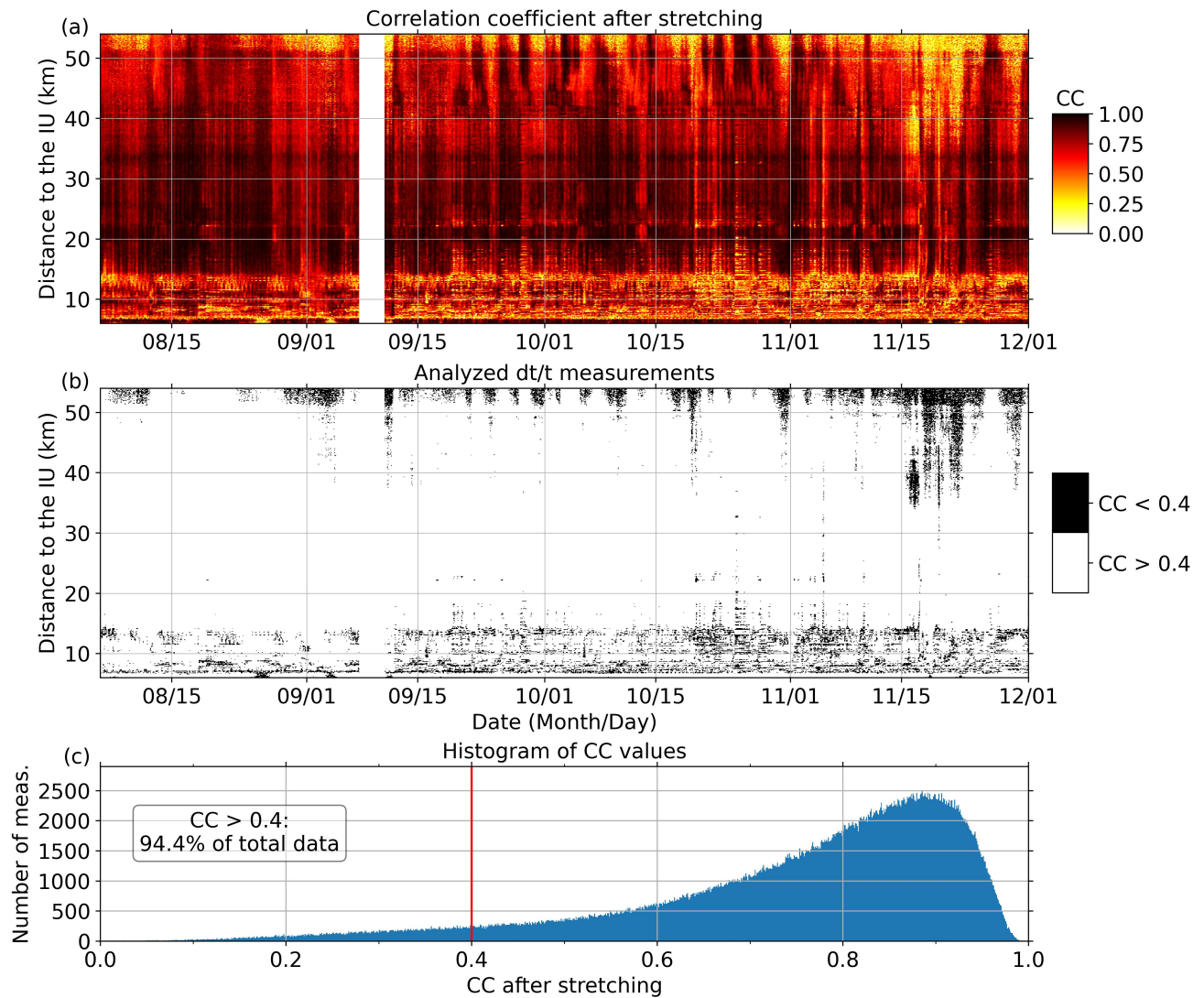
Figure S1. Comparison between the wave height recorded by buoys 46229 (red) and 46050 (black). Buoy 46229 is the closest to the cable, but has a data gap between October 10 and November 14, 2021.
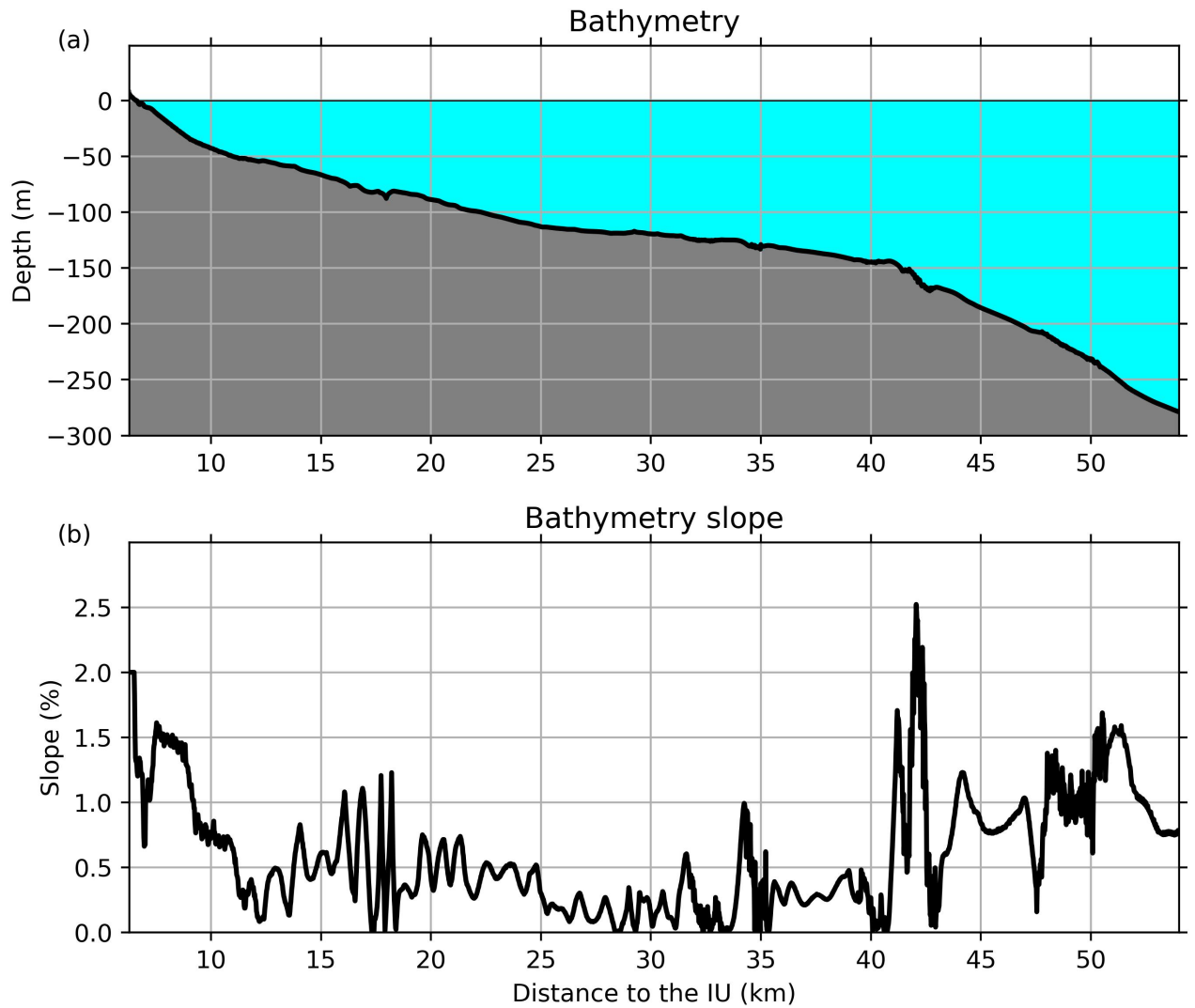
March 13, 2023, 3:52pm

Figure S2. (a) Landward propagating OSGWs obtained after applying a $f - k$ filter to a 10-min strain-rate dataset. (b) Same as (a) for oceanward propagating waves. (c) 10-min CCFs computed using channel 1000 as the virtual source and all the nearby channels as receivers. The dashed red lines determine the quadrant representing landward propagating waves used in this study. Note that only the CCF computed between virtual source 1000 and receiver 985 is used in the analysis of the main manuscript. Same as (c) for oceanward propagating waves.
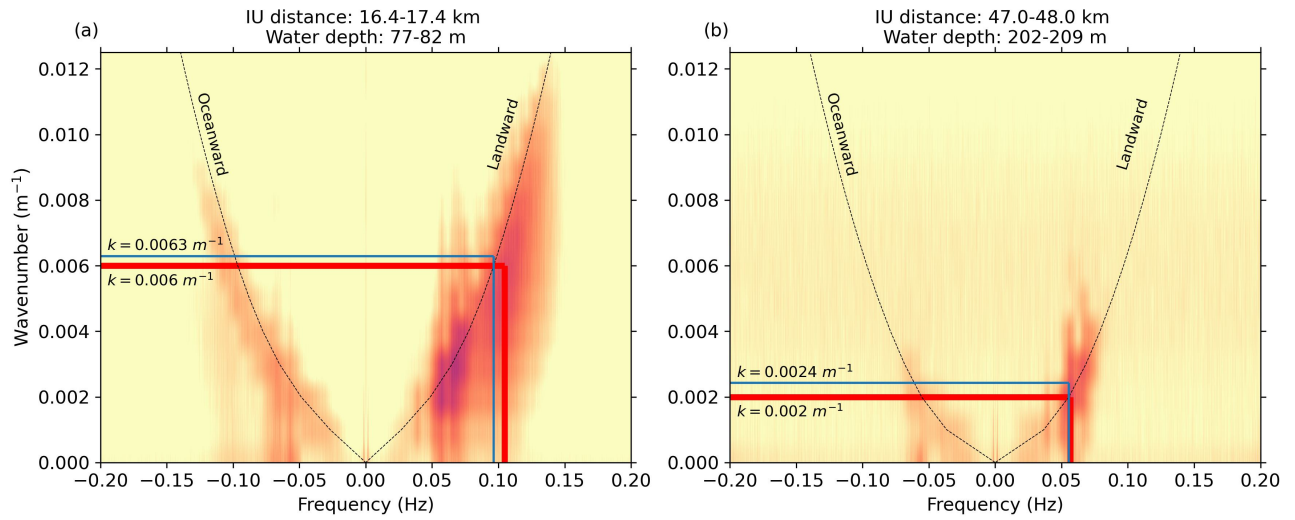
Figure S3. (a) Correlation coefficients (CCs) after stretching for the four months of data along the cable. (b) Binary representation of the selected dt/t measurements for CC after stretching values higher than 0.4. (c) Histogram of CC after stretching values. The vertical red line highlights the CC after stretching value of 0.4.
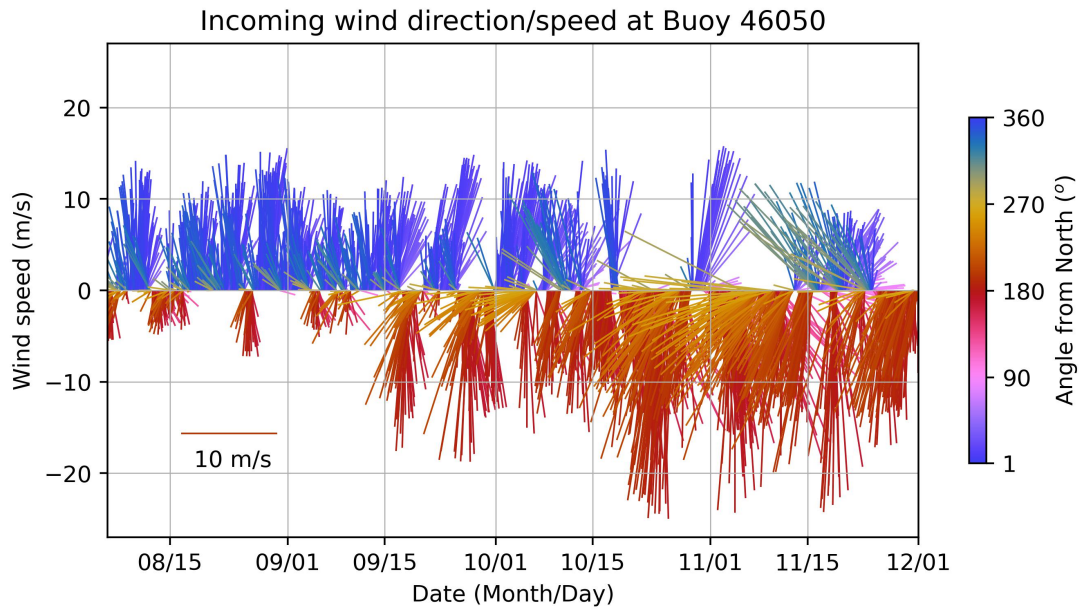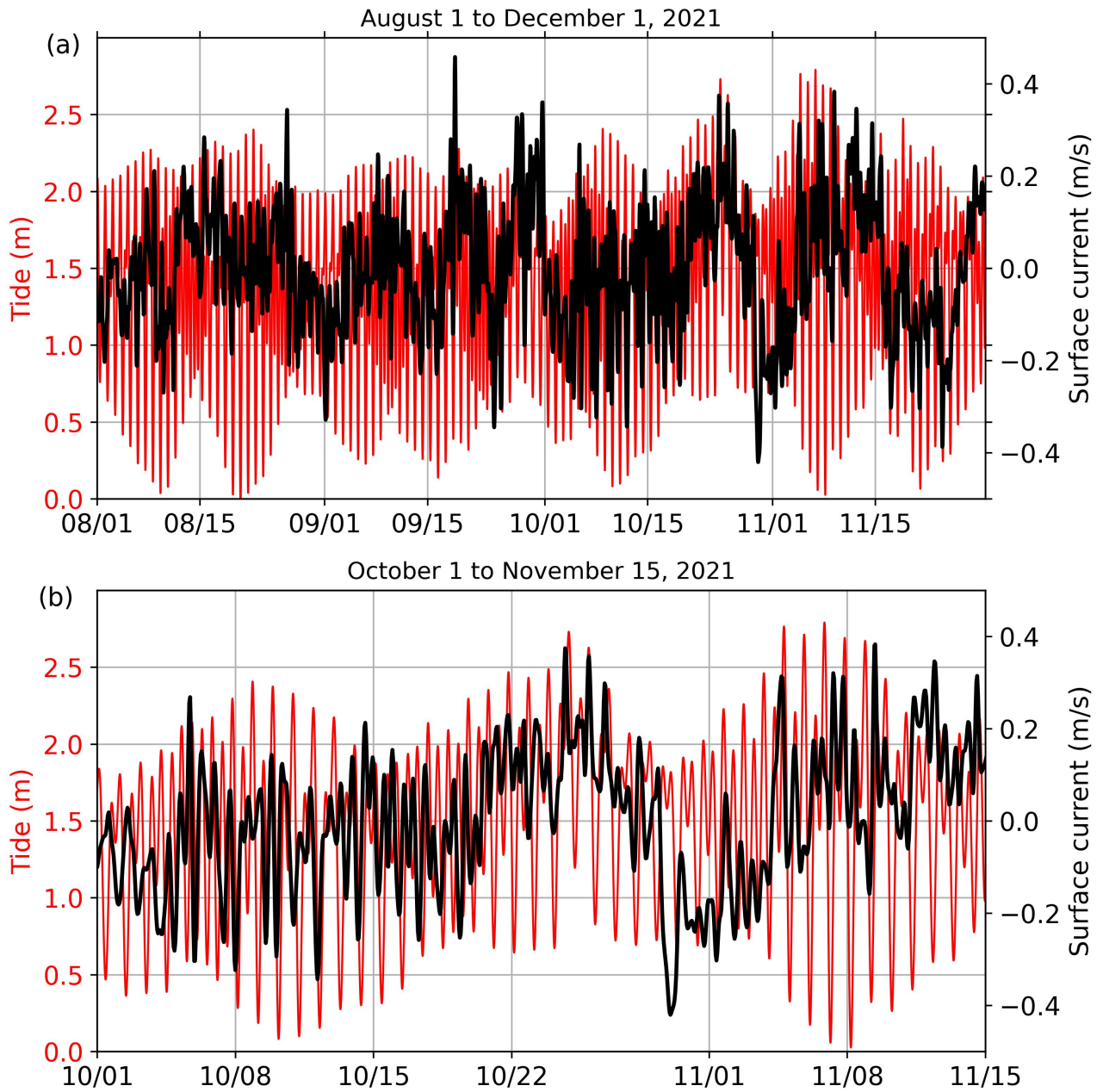
Bathymetry

(a)

Bathymetry slope

(b)

Figure S4. (a) Bathymetry profile along the cable. (b) Slope of the bathymetry profile.

March 13, 2023, 3:52pm

:

Figure S5. (a) Average f-k analysis performed between the data recorded between 16.4 and 17.4 km from the IU over one day of data. The red line highlights the frequency and wavenumber for which the maximum energy is found above 0.1 Hz. The blue line represents the theoretical wavenumber and frequency for a water depth of 79 m. (b) Same as (a) for the data recorded between 47 and 48 km from the IU and a water depth of 206 m.

Figure S6. Hourly wind direction and speed recorded at Buoy 46050. The direction is the direction the wind is coming from in degrees clockwise from the true North, and the length of each line represents the wind speed.

March 13, 2023, 3:52pm

:

August 1 to December 1, 2021

(a)

October 1 to November 15, 2021

(b)

Figure S7. (a) Tide gauge (red) versus high-frequency radar east-west surface current (black) measurements between August 1 and December 1, 2021. (b) Same as (a) between October 1 and November 15, 2021.

March 13, 2023, 3:52pm